Non-precious metal cathodes for anion exchange membrane fuel cells from ball-milled iron and nitrogen doped carbide-derived carbons

Sander Ratso, Andrea Zitolo, Maike Käärik, Maido Merisalu, Arvo Kikas, Vambola Kisand, Mihkel Rähn, Päärn Paiste, Jaan Leis, Väino Sammelselg, et al.

To cite this version:

Sander Ratso, Andrea Zitolo, Maike Käärik, Maido Merisalu, Arvo Kikas, et al.. Non-precious metal cathodes for anion exchange membrane fuel cells from ball-milled iron and nitrogen doped carbide-derived carbons. Renewable Energy, 2021, 167, pp.800-810. 10.1016/j.renene.2020.11.154 . hal-03138163

HAL Id: hal-03138163
https://hal.umontpellier.fr/hal-03138163v1

Submitted on 1 Oct 2021

Non-precious metal cathodes for anion exchange membrane fuel cells from ball-milled iron and nitrogen doped carbide-derived carbons

Sander Ratso[a], Andrea Zitolo[b], Maike Käärik[a], Maido Merisalu[c], Arvo Kikas[c], Vambola Kisand[c], Mihkel Rähn[c], Päärn Paiste[d], Jaan Leis[a], Väino Sammelselg[c], Steven Holdcroft[e], Frédéric Jaouen,[f,*] Kaido Tammeveski[a,*]

[a] *Institute of Chemistry, University of Tartu, Ravila 14a, 50411 Tartu, Estonia*

[b] *Synchrotron SOLEIL, L'orme des Merisiers, BP 48 Saint Aubin, 91192 Gif-sur-Yvette, France*

[c] *Institute of Physics, University of Tartu, W. Ostwald Str. 1, 50411 Tartu, Estonia*

[d] *Institute of Ecology and Earth Sciences, University of Tartu, Vanemuise 46, 51014 Tartu, Estonia*

[e] *Department of Chemistry, Simon Fraser University, 8888 University Drive, Burnaby, BC, V5A 1S6, Canada*

[f] *ICGM, Univ. Montpellier, CNRS, ENSCM, Montpellier, France*

Abstract

Iron and nitrogen doping of carbon materials is one of the promising pathways towards replacing Pt/C in polymer electrolyte fuel cell cathodes. Here, we show a synthesis method to produce highly active non-precious metal catalysts and study the effect of synthesis parameters on the oxygen reduction reaction (ORR) activity in high-pH conditions. The electrocatalysts are prepared by functionalizing silicon carbide-derived carbon (SiCDC) with 1,10-phenanthroline, iron(II)acetate and, optionally polyvinylpyrrolidone, by ball-milling with ZrO_2 in dry or wet conditions, followed by pyrolysis at 800 °C. The catalysts are characterized by scanning and transmission electron microscopy, X-ray photoelectron spectroscopy, X-ray absorption spectroscopy, N_2 physisorption and inductively coupled plasma mass spectrometry. By optimizing the ball-milling conditions, we achieved a reduction in the size of SiCDC grains from >1 μm to 200 nm without negatively affecting the

---

*Corresponding authors. Tel.: +372 7375168; E-mail: kaido.tammeveski@ut.ee (K. Tammeveski).
E-mail: frederic.jaouen@umontpellier.fr (F. Jaouen)

high BET area of catalysts derived from SiCDC. This resulted in increased ORR activity in both rotating disk electrode and anion exchange membrane fuel cell (AEMFC) environments, and improved mass-transport properties of the cathode layer in fuel cell. The ORR activity at 0.9 V in AEMFC of the optimized iron and nitrogen-doped SiCDC reaches 52 mA cm^{-2}, exceeding that of a Pt/C cathode at 36.5 mA cm^{-2}.

***Keywords*:** oxygen reduction, electrocatalysis, carbide-derived carbon, Fe-N$_x$ site, ball-milling, anion exchange membrane fuel cell

1. Introduction

Creating a carbon neutral energy economy while retaining the current lifestyle is one of the most important challenges for the 21st century. Polymer electrolyte membrane fuel cells have emerged as one of the pathways towards reducing the CO$_2$ emissions from automotive applications [1]. In such a fuel cell, the energy from a hydrogen molecule is converted cleanly into electrical energy with water being the only product [2]. Much work has been done in developing proton exchange membrane fuel cells, where the environment is inherently acidic. The main challenge in this field is to reduce the amount of platinum needed to catalyze the sluggish oxygen reduction reaction (ORR) taking place on the cathode, or to replace it entirely with non-precious metal catalysts (NPMCs) [3,4]. Recently, the emergence of highly conductive anion exchange membranes (AEM) has boosted the research of AEM fuel cells (AEMFC), where the pH is elevated [5–10]. In such conditions, the ORR proceeds much faster and thus other, cheaper catalysts can rival or even exceed the activity of platinum-based ones [11,12]. One of the best candidates so far is the class of NPMCs based on iron and nitrogen co-doped nanocarbon materials, labelled FeNC [13–17]. FeNC catalysts can, in turn, be classified into two main categories, depending on the type of Fe-based active sites: Fe-N$_x$ single metal-atom sites, where the iron atom is coordinated to multiple (usually 4) nitrogen atoms [18–22], or metallic iron and/or iron carbide particles covered by nitrogen-doped carbon layers, labelled NC@Fe [11,23–28]. When FeNC catalysts contain exclusively Fe-N_x sites, they are sometimes referred to as single atom catalysts (SAC) [29]. Often, however, pyrolyzed FeNC catalysts comprise both NC@Fe and Fe-N_x sites, in widely different proportions depending on the synthesis, total Fe content and/or subsequent leaching steps. The Fe-N_x moieties are known to catalyze the ORR mostly via a direct four-electron pathway, while the NC@Fe sites reduce oxygen mostly via a 2+2 electron pathway with HO_2^- being the intermediate product of the ORR in alkaline conditions [11,23,24,30]. Recently, the electron density on the central metal atom was found to be a key descriptor for the activity of SACs [31], while the number of carbon overlayers on top of the iron/iron carbide particles has been shown to affect the intrinsic activity of NC@Fe structures. In addition, carbon atoms next to nitrogen atoms doped into the carbon structure also have significant activity towards the ORR, especially in alkaline conditions, with graphitic-N (nitrogen doped into a six-member carbon ring bound to three carbons) and pyridinic-N (nitrogen doped into a six-member carbon ring bound to two carbon atoms) being the most beneficial [20,32–34]. Long-range effects have also been shown to play an important role in the intrinsic ORR activity of NC@Fe and Fe-N_x sites, such as the basicity and degree of graphitization of the N-doped carbon matrix in which these sites are embedded [18,35–37]. In addition to these descriptors controlling the ORR activity, the porous structure of the catalyst has a profound effect on the fuel cell performance. When the latter operates at high current densities not only the ORR kinetics, but also Ohmic losses and especially O_2 mass-transfer losses become important. While micropores are needed in order to reach a high density of Fe-N_x active sites [19,38] a proper balance between micropores and macropores in the FeNC active layer is crucial for efficient mass-transport [39–41].

Carbide-derived carbons (CDC) are carbon materials made by high-temperature chlorination of metal carbides and have the advantage compared to other high-area carbon materials offering a control over the pore size distribution (micropore size in particular) [42,43]. Several CDC-based catalysts have already shown significant ORR catalytic activity in acidic [44–46] or alkaline conditions [26,47]. However, due to the initial particle size of inexpensive carbide precursors, the particle size of the final catalysts shown in the literature to date (average particle diameter >500 nm) has been larger than desired for fuel cell purposes [44]. We have previously studied carbide-derived carbons prepared from Ti, Mo, B, and Si carbides [44,46,48,49], with SiCDC-based catalysts giving very good results in acidic media [49]. Inspired by this, we intend to explore the activity of SiCDC-based catalysts in alkaline media and also in an AEMFC.

In this study, we show a method for drastically reducing the particle size of CDC-based catalysts during the synthesis and doping procedure while retaining a high porosity. The CDC materials are functionalized with 1,10-phenanthroline (Phen) and iron(II) acetate using ball-milling before pyrolysis. It is shown that, in the process, ball-milling not only disperses the Fe and N precursors in CDC but also reduces the CDC particle size, leading to reduced particle size in the final FeNC catalysts. The importance of optimizing the milling step is demonstrated for such CDCs to maximize the electrocatalytic ORR activity.

2. Materials and methods

2.1. Synthesis of iron and nitrogen doped catalysts

Silicon carbide-derived carbon (SiCDC) was supplied by Skeleton Technologies OÜ (Estonia). The SiCDC material (200 mg) was weighed and poured into a ZrO_2 crucible, which contained also either 50 ZrO_2 balls of 5 mm diameter or 20 g of ZrO_2 beads of 0.5 mm diameter. After that, 50 mg of 1,10-phenanthroline (99%, Acros Organics) and 4 mg of iron(II) acetate (95%, Sigma-Aldrich) was added. After this, the crucible was sealed and rotated in a planetary ball-mill (Fritsch Pulverisette 7) at either 100, 200, 400 or 800 rpm with 4 consecutive cycles of 30 min segments and 5 min cool-down periods between each cycle. The catalysts are labelled FeN-SiCDC-x-y, where x is the diameter (in mm) of the ZrO_2 beads and y is the rotation rate of the ball-miller (in rpm). Some materials were ball-milled in the presence of ethanol and these have the suffix (-wet) added to the catalyst name. The steps were as described above, except that 4 ml of ethanol was added, just before sealing the crucible. For one down-selected catalyst (FeN-SiCDC-0.5-400-wet-PVP), 20 mg polyvinylpyrrolidone (PVP) and 4 ml ethanol were added in order to further enhance the ball-milling process. After the ball-milling, all catalyst precursors were sieved to remove the balls, dried and flash pyrolyzed at 800 °C for 1 h in inert atmosphere and quickly removed from the heating zone afterwards.

2.2. Physical characterization of FeN-SiCDC catalysts

Morphology and composition of the catalytic materials were studied with a high-resolution scanning electron microscope (HR-SEM) Helios Nanolab 600 (FEI) and a high-resolution (scanning) transmission electron microscope (HR-(S)TEM) Titan 200, equipped with an energy dispersive X-ray (EDX) Super X detector system (FEI), respectively. The SEM worked with 10 kV and (S)TEM 200 kV primary electron beams, studying the catalytic powder as-received or after their deposition from a suspension to a TEM sample Cu-grid covered by a lacey film, for SEM and (S)TEM analyses, respectively. The bulk content of Fe in the synthesized catalysts was measured using inductively coupled plasma mass spectrometry (ICP-MS, Agilent 8800 ICP-MS/MS). More details on the method are available in our previous work [44].

The N_2 adsorption/desorption analysis was performed at 77 K using the NOVAtouch LX2 analyzer (Quantachrome Instruments). The surface area (S_{dft}) and pore size distribution (PSD) were calculated from N_2 isotherms using a quenched solid density functional theory (QSDFT) equilibrium model for slit-type pores. The total pore volume (V_{tot}) was derived at P/P_0 of 0.97 and the specific surface area (S_{BET}) was estimated with the Brunauer-Emmett-Teller (BET) theory in the interval of P/P_0 values appropriate for microporous materials [50].

X-ray photoelectron spectroscopy (XPS) measurements were conducted using a SCIENTA SES 100 electron spectrometer. For excitation, the Mg K_α radiation (1253.6 eV) from the non-monochromatic twin anode X-ray tube (Thermo XR3E2) was used. All XPS spectra were acquired under ultrahigh-vacuum conditions. The survey scan was collected using the following parameters: energy range, 0–1000 eV; pass energy, 200 eV; step size, 0.5 eV; step duration, 1 s. To measure core-level XPS spectra in the N 1s region, the following parameters were used: energy range 390–410 eV; pass energy 200 eV; step size 0.2 eV; step duration 1 s; number of scans at least 20. The raw data were processed using the Casa XPS software (version 2.3.17). Data processing involved removal of K_α and K_β satellites, correction with electron spectrometer transmission function and peak fitting using the Gauss–Lorentz hybrid function GL 70 (Gauss 30%, Lorentz 70%) and Shirley-type backgrounds.

X-ray absorption spectroscopy (XAS) data were collected at the Fe K-edge in fluorescence geometry at the SAMBA beamline of the synchrotron SOLEIL (France) using a sagittally bent double crystal Si(220) monochromator and a Canberra 35-elements germanium detector. Data treatment and linear combination fitting were performed with the Athena software [51].

2.3. Electrode preparation and electrochemical characterization

The electrocatalytic activity of the FeN-SiCDC catalysts was measured with the rotating disk electrode (RDE) method. The catalyst materials were dispersed in ethanol into which 1 µl of 2 wt.% aQAPS S-14 ionomer solution (Hephas Energy, China) was added per mg of catalyst. The suspension with a concentration of 2 mg_{FeNC} cm^{-3} was then coated onto a glassy carbon (GC, GC-20SS, Tokai Carbon, Japan) tip of 0.2 cm^2 geometric area in a sequence of 1 μl, then 2 times 2 μl and then 4 times 4 μl, giving a total loading of 200 μg cm^{-2}. The electrodes were dried using rotation and inserted into an electrochemical cell containing O_2-saturated (99.999%, AGA) 0.1 M KOH solution. A saturated calomel electrode (SCE) connected via Luggin's capillary served as the reference electrode and a glassy carbon rod was used as the counter electrode. All the potentials in this work are however reported vs. the reversible hydrogen electrode (RHE) and the conversion from SCE to RHE was made by calibrating the reference electrode used. The potential was converted with the following formula: $E_{\mathrm{RHE}} = E_{\mathrm{SCE}} + 1.008$ V.

The catalyst-coated electrodes were pre-conditioned via 10 cyclic voltammograms from 1.0 to -0.2 V vs. RHE at a scan rate (ν) of 100 mV s^{-1}. The ORR activity was measured at different electrode rotation rates (ω) using staircase voltammetry with a step of 25 mV and a dwell time of 15 s. A PGSTAT30 Autolab potentiostat/galvanostat (Metrohm Autolab, The Netherlands) with NOVA 2.0 software was used to control the experiments. A CTV101 speed control unit connected to an EDI101 rotator (Radiometer) controlled the electrode rotation rate.

2.4. MEA fabrication and fuel cell measurement

Membrane-electrode assemblies (MEAs) for AEMFC measurements were prepared by first dispersing the catalyst in a 3:1 mixture (by volume) of methanol:Milli-Q water. The mixture contained 1 wt.% total of solids, which in turn was comprised of 85% catalyst and 15% of hexamethyl-*p*-terphenyl poly(benzimidazolium) ionomer (HMT-PMBI) [52]. The dispersion was sonicated for 1 h, after which it was pipetted onto a Freudenberg H23C4 gas diffusion layer (GDL) of geometric area of 5 cm^2 in 200 μl aliquots (multiple droplets of the solution were deposited). The loading of FeN-SiCDC catalyst on the cathode was 2 mg cm^{-2}. PtRu/C catalyst (Alfa Aesar HiSPEC™ 12100 50 wt.% Pt, 25 wt.% Ru), with a loading of 0.8 mg_{PtRu} cm^{-2} on Freudenberg H23C4 GDL was used as the anode. For reference, 46.1 wt.% Pt/C (TKK, Japan), was also tested as the cathode. The ink formulation and electrode preparation procedure for the anode was the same as for the cathode. The electrodes and the HMT-PMBI membrane were soaked in 1 M KOH solution for 1 day prior to testing and then installed into a 5 cm^2 single cell (Fuel Cell Technologies, Inc., USA) and the cell assembled with a torque of 7 N m. The single cell fuel cell performance was evaluated at the cell temperature of 60 °C with Greenlight Fuel Cell Test Station (G50 Fuel cell system, Hydrogenics, Vancouver, Canada). Fully humidified oxygen (0.2 NLPM) and 82% RH hydrogen (0.4 NLPM) were fed into the cell with a backpressure of 200 kPa.

3. Results and discussion

3.1. Physical characterization of the pristine SiCDC and FeN-SiCDCs

3.1.1 Effect of ball-milling on the physical characteristics of FeN-SiCDCs

Figure 1 illustrates with SEM the effect of ball-milling on the particle size of the catalysts, after pyrolysis. Figure 1a shows a SEM image of the catalyst obtained by pyrolysis (same conditions as the other samples) of the FeN-SiCDC-wet precursor material. The latter was obtained by mixing SiCDC, Phen and iron(II) acetate in ethanol using simply sonication and followed by drying. A variety of particle sizes is shown with large catalyst particles (diameter higher than 1 μm) dominating and some particles with a diameter over 10 μm also visible. For the same composition of the catalyst precursor (same ratios of SiCDC, Phen and iron(II) acetate) but after ball-milling with 5 mm ZrO_2 beads followed by pyrolysis (FeN-SiCDC-5-400, Figure 1b), one can see that the average grain size has decreased somewhat, with a higher fraction of particles in the range of 1 μm vs. those in the range of 5-10 μm in Figure

1a. The particles in FeN-SiCDC-5-400 are also rounder than those in the SiCDC pristine material and in the FeNC catalyst obtained without milling the precursors. Increasing further the ball-milling rotation rate to 800 rpm in dry conditions and with 5 mm ZrO_2 beads only slightly decreased the particle size of the final catalyst (Figure S1b). In contrast, a significant effect from using smaller ZrO_2 beads and in wet conditions (ethanol) can be seen in Figure 1c for the catalyst FeN-SiCDC-0.5-400-wet. It must be noted that milling in dry conditions with 0.5 mm beads has, however, negligible effect on the particle sizes because the balls tend to get stuck in the soft precursor mixture and not grind efficiently (Figure S1a). This is the reason why, in a following attempt, ethanol was added to allow for movement of the beads. In those conditions, the ball-milling becomes very effective, as the particle sizes seen in Figure 1c and in the close-up in Figure 1d are much smaller than those achieved with 5 mm beads without added ethanol. In Figure 1d, the smooth surface morphology of the particles can also be seen. However, the particle sizes are still quite varied and a significant fraction of particles have a size >1 μm, not ideal for ink preparation and for cathode layer structure. Figures 1e,f show SEM images of the FeNC catalyst prepared in similar conditions (i.e. with added ethanol) but also in addition using PVP, labelled FeN-SiCDC-0.5-400-wet-PVP. Using a surfactant such as PVP further helps to separate smaller particles formed during the ball-milling and to enhance the milling itself, thereby giving a more uniform particle size of <1 μm. This represents a significant breakthrough since decreasing the grain size of CDC-based catalysts to such extent has hitherto been a challenge [26,44,53]. The rough surface structure of the FeN-SiCDC-0.5-400-wet-PVP catalyst is shown with SEM at higher magnification in Figure 1f, suggesting these particles are also highly porous.

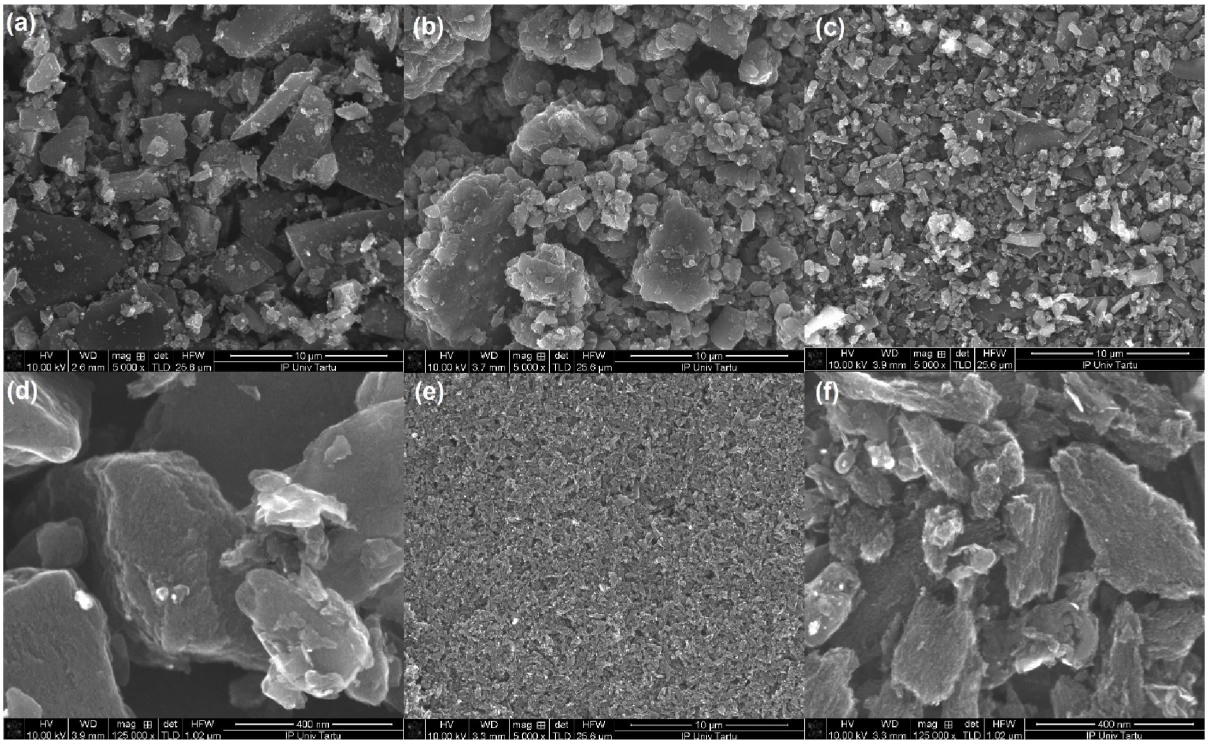

Figure 1. SEM micrographs of the FeNC catalysts obtained after same pyrolysis conditions but different milling conditions (a) FeN-SiCDC-400-wet, (b) FeN-SiCDC-5-400, (c,d) FeN-SiCDC-0.5-400-wet and (e,f) FeN-SiCDC-0.5-400-wet-PVP.

The structure of FeN-SiCDC-0.5-400-wet-PVP was further investigated by TEM and HAADF-STEM (Figure 2). In Figure 2a, particles with sizes ranging from tens of nanometers to hundreds of nanometers can be seen along with some denser particles. Figure 2b shows the surface of the catalyst, with amorphous carbon as well as bright nanometric clusters and bright single dots of atoms with higher atomic mass than carbon also visible. The nanosize clusters in this image are identified by EDX mapping to be rich in Zr and O (Figure 2e-f). We assign them therefore to ZrO_2 particles coming from the beads and/or the walls of the crucible used for the milling. In contrast, the bright dots uniformly distributed over the whole mapped area can be assigned to Fe atoms in Fe-N_x sites as suggested also by the uniform distribution of N atoms (Figure 2c-d).

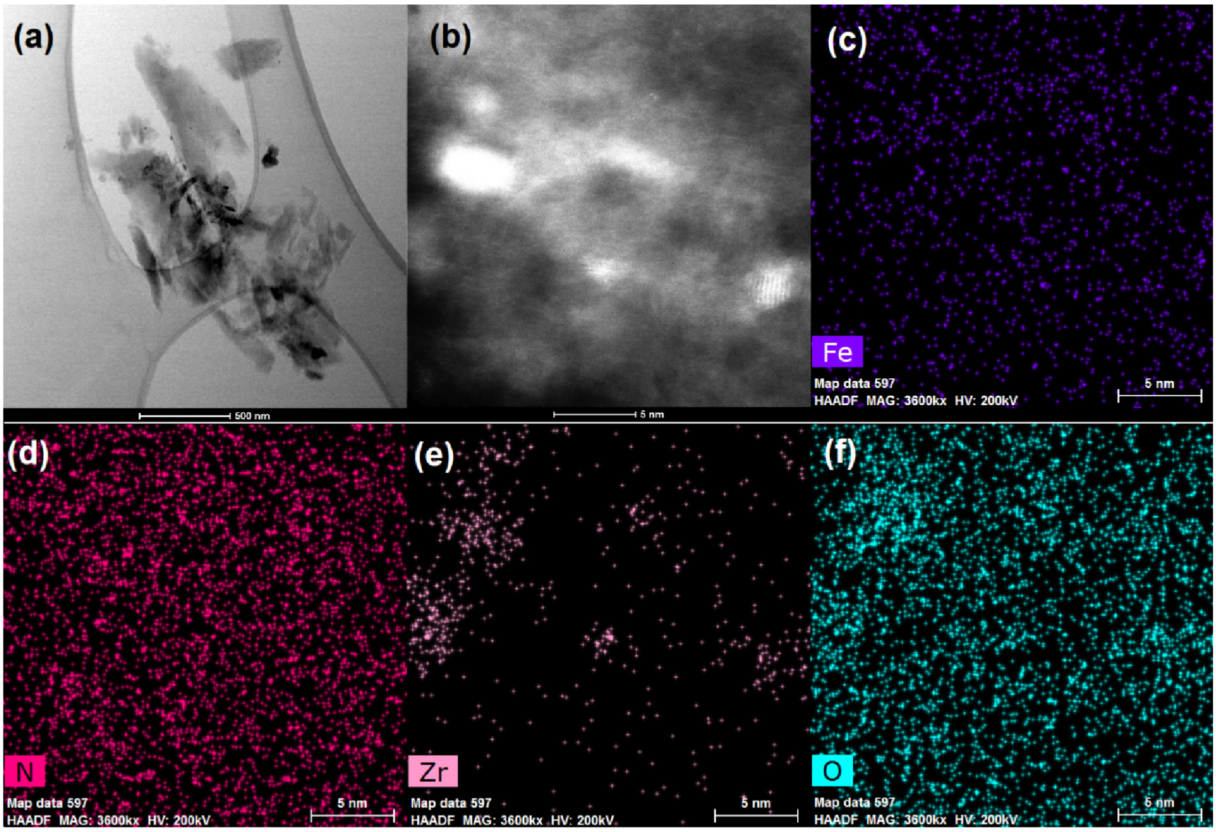

Figure 2. (a) TEM and (b) HAADF-STEM images of the catalyst FeN-SiCDC-0.5-400-wet-PVP with (c-f) EDX elemental mapping images from the area shown in (b).

Figure 3a compares the X-ray absorption near-edge structure (XANES) spectra of the four FeNC catalysts of the present study with that of a reference FeNC material comprising only Fe-N$_x$ sites (labelled Fe$_{0.5}$), whose active-site structure was identified in our previous study [18]. The comparison reveals a similar XANES fingerprint for FeN-SiCDC-5-400, FeN-SiCDC-0.5-400, FeN-SiCDC-0.5-400-wet and Fe$_{0.5}$, while FeN-SiCDC-0.5-400-wet-PVP has a slightly different spectrum that can be a result of a minor presence of Fe-based nanoparticles along with Fe-N$_x$ sites (see Figure S4 of ref. 18). The fully atomically dispersed nature of Fe in FeN-SiCDC-5-400, FeN-SiCDC-0.5-400 and FeN-SiCDC-0.5-400-wet was confirmed by extended X-ray absorption fine structure (EXAFS) spectroscopy. The Fourier transform of the EXAFS spectra (Figure 3b) of the four catalysts of this study reveals a main peak around 1.4 Å (not corrected for the phase shift) assigned to the Fe-N first coordination shell, while a reduction of the intensity of the first-shell peak and the appearance of Fe-Fe contributions for

FeN-SiCDC-0.5-400-wet-PVP vs. all other catalysts of the present study indicates the coexistence of FeN_x moieties with metal-based nanoparticles. A linear combination fitting of the FeN-SiCDC-0.5-400-wet-PVP XANES spectrum was carried out using the XANES spectra of FeN-SiCDC-0.5-400-wet (the catalyst prepared identically except for the absence of PVP during milling) and metallic Fe foil as references. As shown in Figure 3c the spectrum of FeN-SiCDC-0.5-400-wet-PVP is well reproduced by linear addition of the two reference components, with a relative Fe proportion of 92% of Fe-N_x sites and 8% of metallic iron.

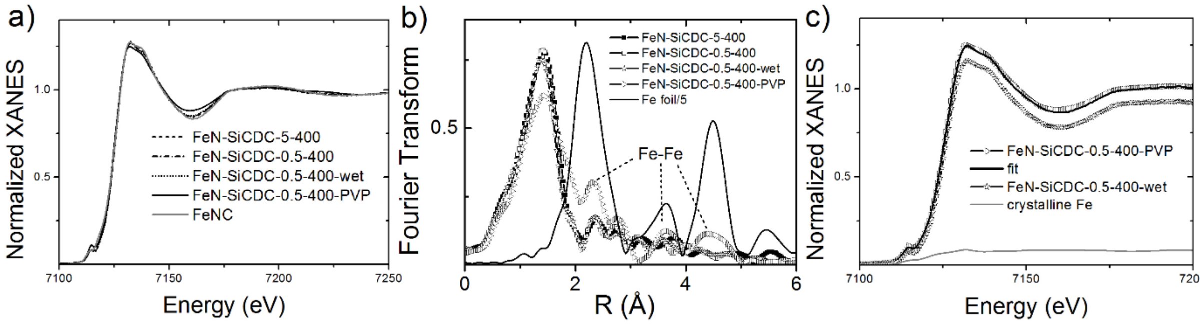

Figure 3. XAS characterization of FeNC catalysts. (a) Comparison between the Fe K-edge XANES experimental spectra of FeN-SiCDC-5-400 (dashed line), FeN-SiCDC-0.5-400 (dash-dotted line), FeN-SiCDC-0.5-400-wet (dotted line), FeN-SiCDC-0.5-400-wet-PVP (black line) and FeNC (grey line) from ref. [15]. Note that all the spectra, except for the spectrum of FeN-SiCDC-0.5-400-wet-PVP, are nearly identical. (b) Phase-uncorrected Fourier transform of the experimental EXAFS spectra of the FeN-SiCDC catalysts and the crystalline metallic Fe foil (for the latter, the signal is divided by a factor 5 for easier comparison). (c) Linear combination fitting of the Fe k-edge XANES spectra of FeN-SiCDC-0.5-400-wet-PVP using the XANES spectra of FeN-SiCDC-0.5-400-wet and of a metallic Fe foil as fitting spectral components.

The porosity in the FeNC catalysts of the present study were then investigated with N_2 physisorption and compared to those of the SiCDC pristine material. The pore size distributions calculated from the N_2 adsorption-desorption isotherms via the QSDFT model are shown in Figure 4 and the calculated textural properties are given in Table 1.

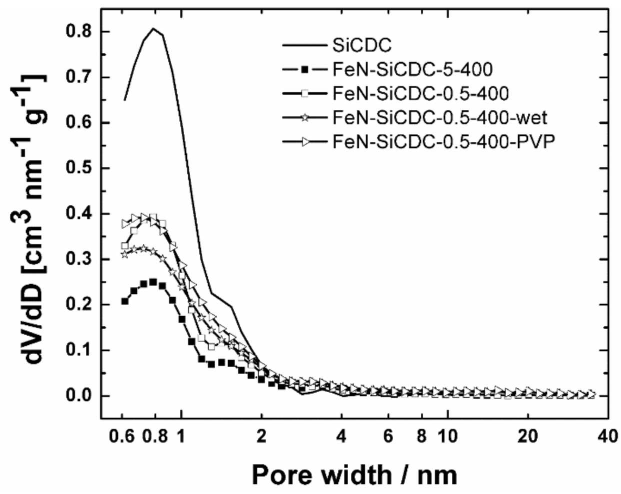

Figure 4. Pore size distributions for the pristine SiCDC and for the four FeN-SiCDC catalysts.

Using 5 mm zirconia balls and dry milling, the specific surface area of the final catalyst decreased more than 3 times when compared to the starting CDC material (458 and 1363 m^2 g^{-1}, respectively, Table 1). This is similar in magnitude to the effect we previously observed with 5 mm balls at the same rotation rate, which serves as a starting point [49]. Changing the diameter of the zirconia balls from 5 to 0.5 mm reduced the losses in S_{BET} by a third, resulting in a catalyst with a BET area of 709 m^2 g^{-1} for FeN-SiCDC-0.5-400 compared to 458 m^2 g^{-1} for FeN-SiCDC-5-400. This effect of the size of the zirconia balls on the specific surface area of the final FeNC catalyst is similar if the milling is performed in ethanol (FeN-SiCDC-0.5-400-wet has a BET area of 735 m^2 g^{-1}). However, the pore size distributions of FeN-SiCDC-0.5-400 and FeN-SiCDC-0.5-400-wet are somewhat different (Figure 4), with less volume of pores having a diameter under 1 nm when using wet milling. This probably implies that more micropores of the pristine SiCDC were closed in wet vs. dry milling conditions. Thus, with the different milling conditions investigated here, we identify that resorting to small zirconia beads and combined with wet milling is beneficial for reducing catalyst particle sizes.

Surfactants are known to decrease agglomeration of milled particles and their sticking to the milling jar and milling media, meaning that the final particle size achieved can be smaller [54]. When adding PVP during the milling with small zirconia beads and in wet conditions, the BET surface area of the resulting FeNC is maximum, reaching 865 m^2 g^{-1} (FeN-SiCDC-0.5-400-wet-PVP, Table 1). The loss of BET area compared to SiCDC is thus minimized to *ca* 40%. In our previous study, we determined that when iron(II) acetate and Phen are dispersed on SiCDC without ball-milling, the S_{BET} loss is also around 40%, due to the blocking or filling of some micropores of SiCDC with the new carbon phase derived from Phen during pyrolysis [49]. This means that wet milling with 0.5 mm ZrO_2 balls and added PVP in ethanol can completely avoid the negative effect of ball-milling on the BET area.

Table 1. Textural properties of FeN-SiCDC catalysts as determined by BET analysis.

Catalyst	S_{BET}, m^2 g^{-1}	S_{DFT}, m^2 g^{-1}	V_{tot}, cm^3 g^{-1}	$V_{\mu(t\text{-}plot)}$, cm^3 g^{-1}	$V_{\mu(DFT)}$, cm^3 g^{-1}
SiCDC	1363	1346	0.688	0.60	0.57
FeN-SiCDC-5-400	458	455	0.296	0.2	0.18
FeN-SiCDC-0.5-400	709	701	0.43	0.31	0.28
FeN-SiCDC-0.5-400-wet	735	710	0.55	0.24	0.28
FeN-SiCDC-0.5-400-wet-PVP	865	835	0.62	0.28	0.33

3.2 Elemental content in FeN-SiCDCs

The bulk elemental content of the FeN-SiCDC catalysts was measured via ICP-MS. The iron content is near 0.5 wt.% for all the catalysts, while significant amounts of Zr is also present. The source of Zr is ZrO_2 from the crucible and the balls used for ball-milling. SiC cores are also seen in the center of some SiCDC particles (Figure 2a), implying that the chlorination used to prepare SiCDC from SiC was incomplete. It is suggested that the residual SiC renders the SiCDC material harder than carbon, or that SiC cores are separated from SiCDC grains during the milling, eroding the ball-milling apparatus since SiC is an extremely hard material and thereby explaining the presence of significant amount of Zr in the catalysts. ZrO_2 is present as nanoparticles on the catalyst surface as can be seen from the TEM images (Figure 2). However, in our previous studies, we could exclude the ZrO_2 nanoparticles from having a large effect on the high ORR activity observed for the present CDC-based FeNC catalysts [26,44,49].

Table 2. Fe and Zr contents in the FeN-SiCDC catalyst materials as determined by ICP-MS.

Catalyst	Fe		Zr	
	wt.%	+/- wt%	wt.%	+/- wt%
FeN-SiCDC-5-400	0.506	0.015	2.703	0.027
FeN-SiCDC-0.5-400	0.424	0.010	0.260	0.008
FeN-SiCDC-0.5-400-wet	0.430	0.008	4.735	0.123
FeN-SiCDC-0.5-400-wet-PVP	0.503	0.008	3.791	0.099

The surface elemental composition of the FeN-SiCDC catalysts was analyzed by XPS, with the most important results shown in Figure 5 (N1s core-level spectra deconvoluted according to [20]) and in Table 3. An essential factor towards the ORR activity is the nitrogen content and speciation. It can be seen that decreasing the zirconia ball size while keeping other ball-milling conditions the same increased the overall N content by about 0.5 at.% (compare FeN-SiCDC-0.5-400 vs FeN-SiCDC-5-400 in Table 3).More importantly, the increased N content is assigned to the ORR-active Fe-N_x and pyridinic-N components. Introducing ethanol during the ball-milling significantly lowered the total N content from ca 4 to 2 at.% (FeN-SiCDC-0.5-400 vs. FeN-SiCDC-0.5-400-wet in Table 3), but also had an important impact on the nitrogen speciation: the overall N content was divided by two, however the Fe-N_x content was kept at a reasonably high level (0.72 at.%). The negative effect when ball-milling in wet conditions on the total N content however was avoided when wet milling was done in the presence of PVP. FeN-SiCDC-0.5-400-wet-PVP has 4.5 at.% N, comparable or even higher than the N content of FeNC catalysts prepared via dry milling. Simultaneously, FeN-SiCDC-0.5-400-wet-PVP shows a higher nitrogen content engaged in Fe-N_x sites, 1.47 at.%.

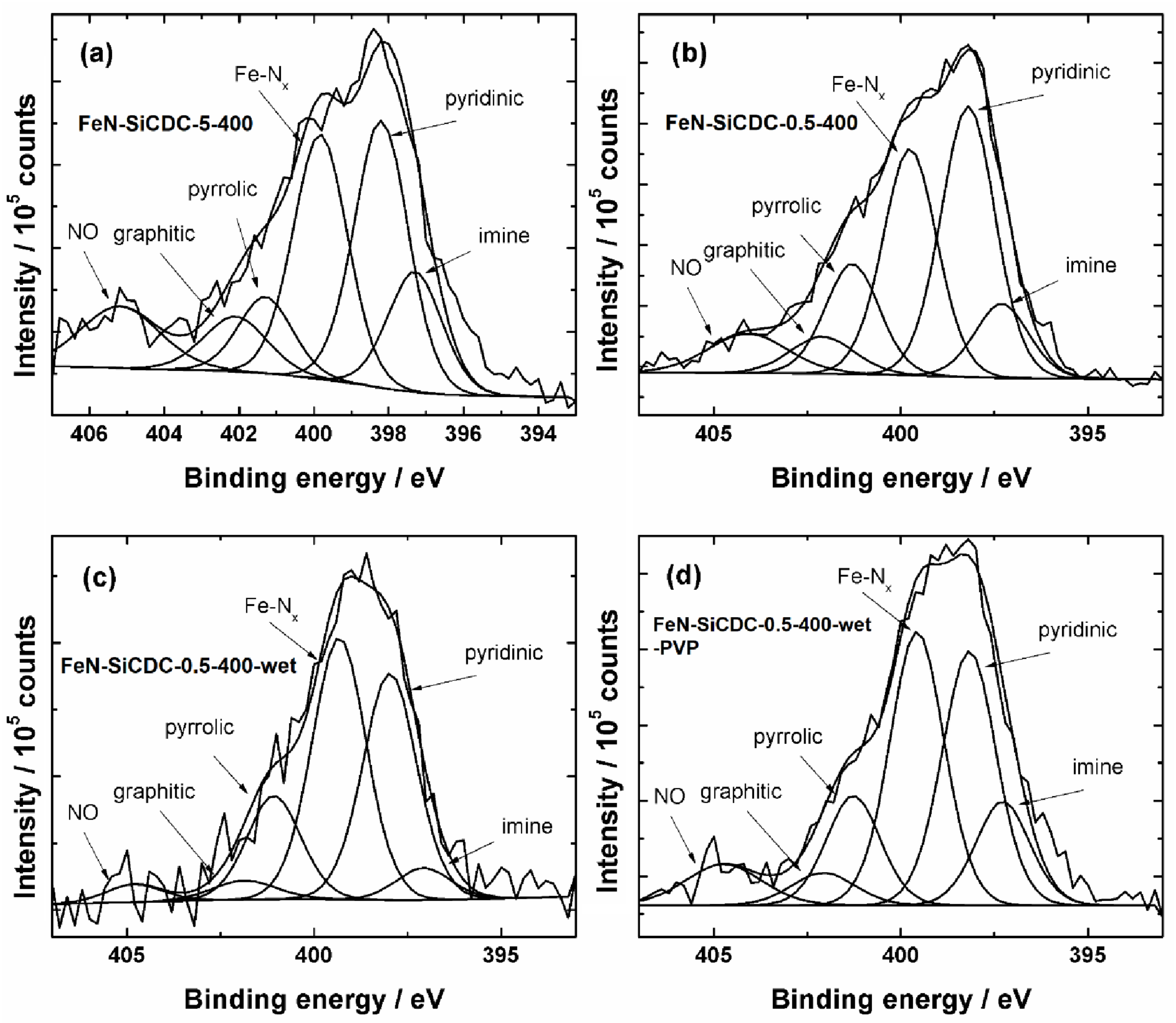

Figure 5. XPS N1s core-level spectra for (a) FeN-SiCDC-5-400, (b) FeN-SiCDC-0.5-400, (c) FeN-SiCDC-0.5-400-wet and (d) FeN-SiCDC-0.5-400-wet-PVP.

Table 3. Surface elemental composition and nitrogen speciation of the FeN-SiCDC catalysts.

Atomic concentration per element, or per N species	FeN-SiCDC-5-400	FeN-SiCDC-0.5-400	FeN-SiCDC-0.5-400-wet	FeN-SiCDC-0.5-400-wet-PVP
C at.%	90.22	89.14	89.32	86.62
O at.%	6.27	6.9	8.68	8.63
N at.%	3.5	3.94	2.01	4.5
Pyridinic N at.%	1.08	1.36	0.68	1.36
Imine at.%	0.49	0.37	0.1	0.56
Fe-N$_x$ at.%	0.99	1.14	0.79	1.47
Pyrrolic N at.%	0.31	0.56	0.31	0.59
Graphitic N at.%	0.26	0.22	0.07	0.21
NO at.%	0.37	0.29	0.06	0.31

3.3. Electrocatalytic activity of FeN-SiCDC catalysts towards the ORR

3.3.1. Effects of different ball size on the ORR activity of FeN-SiCDC catalysts

For evaluating the ORR activity of the prepared FeN-SiCDC catalysts, the first method used was RDE. Figure 6 shows a comparison of the electrocatalytic activity of catalysts made by ball-milling a mixture of SiCDC, Phen and iron(II) acetate using ZrO_2 beads of different sizes and conditions in O_2-saturated 0.1 M KOH solution. Because increasing the rotation rate of the ball-mill during synthesis over 400 rpm only decreased the particle size of the final FeN-SiCDC catalysts somewhat, while bringing with itself more negative effects such as the large decrease in specific surface area and destruction of the surface structure, which decreased the ORR activity, smaller beads were used as an alternative. Decreasing the ball size in a ball-mill is a known way to decrease the particle size of the final product. Because a smaller particle size also increases the external surface area of a catalyst, this can lead to an increase in the ORR electrocatalytic activity, especially in a fuel cell where mass-transfer is complicated in highly microporous materials such as the SiCDC-based catalysts presented here. Figure 6 shows the ORR activity of catalysts prepared by ball-milling and pyrolysis at 400 rpm with both 5 and 0.5 mm balls employing dry and wet milling. The kinetic current density (j_k) achieved at 0.9 V using dry milling was 1.2 mA cm^{-2}, over two times lower than when using 5 mm balls. However, when ethanol was added to the precursors to create a motor-oil like viscous mixture into the crucible, the effects were much more beneficial. The precursors are much better mixed as a result and as can be seen from the SEM images, the particle size is much decreased. This carries on to the ORR activity: the j_k value at 0.9 V vs RHE for FeN-SiCDC-0.5-400-wet catalyst is 2.8 mA cm^{-2}. The wet milling with smaller balls and PVP also managed to eliminate the negative effect on the S_{BET} of the catalyst from ball-milling. This addition has a profound effect on the ORR activity as can be seen from Figure 6. The j_k for FeN-SiCDC-0.5-400-wet-PVP is 3.8 mA cm^{-2}, which is the highest in this work and even surpassed that of commercial Pt/C (j_k = 2.3 mA cm^{-2} at 0.9 V). To elucidate whether or not simply using ethanol and PVP to disperse the precursors without any ball-milling also has the same effect, a FeN-SiCDC-wet catalyst was synthesized by simply sonicating SiCDC, iron(II)acetate, PVP and Phen in a beaker containing ethanol, which was then dried and pyrolyzed at the same conditions as the other catalysts. As can be seen from Figure 6 and Table 4, the ball-milling of the catalyst at 400 rpm with 5 mm balls already increases both the onset potential, kinetic current density at 0.9 V and the diffusion-limited current density, so there is definitely a profound effect from the ball-milling on both descriptors. The increase in the kinetics at 0.9 V is regarded as a true effect of improved activity, while the increased diffusion-limited current density may be a true effect of increased selectivity for four-electron reduction, or more simply may reflect a more uniform and complete coverage of the GC disk by the catalyst ink. Improved ink dispersion was visible after the milling, which probably resulted in a more complete coverage of GC than without any ball-milling. Assuming same or similar ORR selectivity, an incomplete coverage of GC would result in a lower diffusion-limited current density, proportional to the coverage ratio.

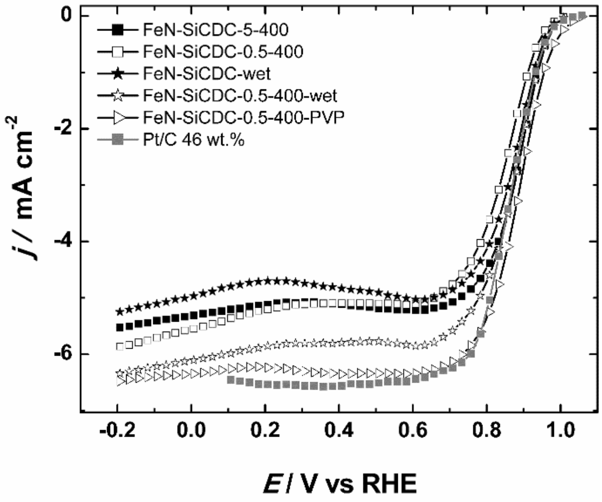

Figure 6. Steady-state ORR polarization curves for the FeN-SiCDC catalysts using different ball-milling conditions and a commercial Pt/C catalyst recorded in O_2-saturated 0.1 M KOH. ω = 1900 rpm. The catalyst loading is 0.2 mg cm^{-2} for the NPMCs and 46 μg_{Pt} cm^{-2} for Pt/C.

3.3.2. Effects of rotation rate of the ball-mill on the ORR activity of FeN-SiCDC catalysts

Figure 7 shows a comparison of the ORR electrocatalytic activity of catalysts made by ball-milling a mixture of SiCDC, Phen and iron(II) acetate using different rotation rates of the ball-mill in O_2-saturated 0.1 M KOH solution. For the 100 rpm ball-milled catalyst, the kinetic current density at 0.9 V was 0.7 mA cm^{-2} (Table 4). Raising the rotation rate of the ball-mill to 400 rpm increased the j_k value to 2.9 mA cm^{-2}. At 800 rpm, however, j_k at 0.9 V decreased to 0.6 mA cm^{-2}, likely due to the CDC surface structure being destroyed by the high impact ball-milling. Using no ball-milling at all and instead sonicating the reactants in ethanol to disperse them followed by drying prior to the pyrolysis step resulted in the j_k value of 2.2 mA cm^{-2}. The porosity of the final catalyst decreases as well at higher rotation rates [49], which in turn also counteracts the positive effects of the milling. Pyrolysis of carbon materials in the presence of a nitrogen source (Phen) and an iron source is known to create ORR-active sites [26,44,55,56]. In this case iron(II) acetate and Phen form the Fe(Phen)$_3$ complex [57]. The Phen ligands protect the Fe atoms from agglomerating during the pyrolysis step, thereby leading to more Fe-N$_x$ sites than iron/iron carbide nanoparticles. As the rotation rate of the ball-mill increases, the dopants are better dispersed onto the carbon material, which itself is also ground into smaller particles with increasing rotation rate. A better dispersion of the precursors also leads to more separation between the Fe atoms. Thus, 400 rpm is selected as the optimum rotation rate for the ball-mill.

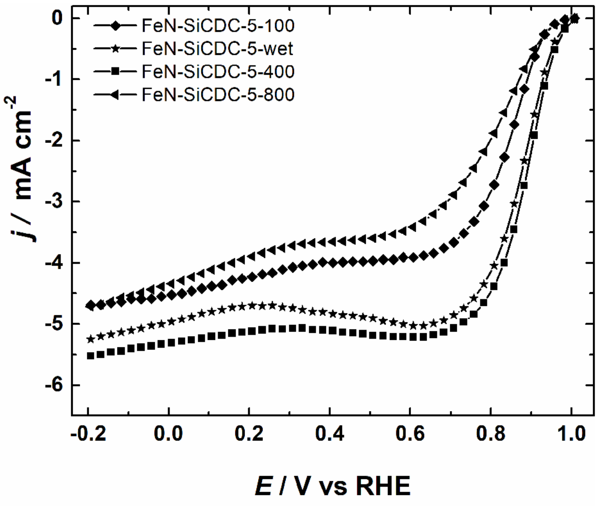

Figure 7. Steady-state ORR polarization curves for the FeN-SiCDC catalysts synthesized using 5 mm ZrO_2 balls and different rotation rates for the dry ball-milling and one sample where the reactants were dispersed in ethanol. Polarization curves were recorded in O_2-saturated 0.1 M KOH solution. ω = 1900 rpm.

3.3.3 AEMFC performance using FeN-SiCDC cathode catalysts

For testing the *in situ* activity of the FeN-SiCDC, catalyst-based MEAs with different cathodes and a PtRu/C anode with a HMT-PMBI membrane were sandwiched in a fuel cell as described in the Experimental section. Figure 8 and Table 4 show the results of the AEMFC testing. FeN-SiCDC-5-400, which had the largest particle size, performs the worst at both higher potentials and at higher current densities, with the current density at 0.9 V being 10.3 mA cm^{-2} and the maximum power density (P_{max}) achieved 282 mW cm^{-2}. Using 0.5 mm ZrO_2 beads for wet ball-milling increased the fuel cell performance significantly, with the j at 0.9 V being 36.2 mA cm^{-2} and the P_{max} of 333 mW cm^{-2} for the FeN-SiCDC-0.5-400-wet catalyst. This is likely due to the smaller particle size and better dispersion of the catalyst precursors as well as retaining more surface area than FeN-SiCDC-5-400. A smaller particle size is also beneficial for O_2 transport and ionomer access to the active sites, which increases the performance at both high potentials and high current densities. Adding PVP to the precursor mixture enhanced the activity even more, with FeN-SiCDC-0.5-400-wet-PVP showing 52 mA cm^{-2} at 0.9 V and P_{max} of 356 mW cm^{-2}. The XPS results showed that the catalyst with added PVP also had the highest elemental contents of nitrogen, especially that of the ORR-active moieties in the near-surface layers, which is an important contributor to the high electrocatalytic activity of this catalyst. This is especially impressive when compared to the respective values obtained with the commercial 46 wt.% Pt/C cathode catalyst (36.5 mA cm^{-2} and 352 mW cm^{-2}). A comprehensive comparison with other Fe-N-C catalysts utilized as cathode materials in AEMFCs from the literature is given in Table S1 [10,48,58-85]. This comparison shows that the FeN-SiCDC-0.5-400-wet-PVP catalyst has the second highest ORR activity at 0.9 V and 60°C in fuel cell, only surpassed by a catalyst labelled as NH_3-

activated Fe-N-C (80-90 mA cm^{-2} at 0.9 V) [10]. Even considering the peak power density (which depend on many other factors than the sole cathode catalyst ORR activity), the results obtained in this work are surpassed by only five other reports on Fe-N-C cathodes, obtained with more advanced commercial or developmental ionomers and/or AEMs [10,77–79,82]. It is well known in the field that the ionomer morphology and AEM properties (thickness, conductivity, water management) affect to an enormous extent the performance of AEMFCs at high current density [5,10,86], while the accuracy of the humidity control by different fuel cell test stations plays an additional role. Therefore, based on the ORR activity at 0.9 V and the internal comparison to a Pt/C cathode with same AEM and AEI and in a same fuel cell test station in the present work, it is clear that the FeN-SiCDC-0.5-400-wet-PVP catalyst is a promising alternative to the commercial Pt/C catalyst in AEMFC.

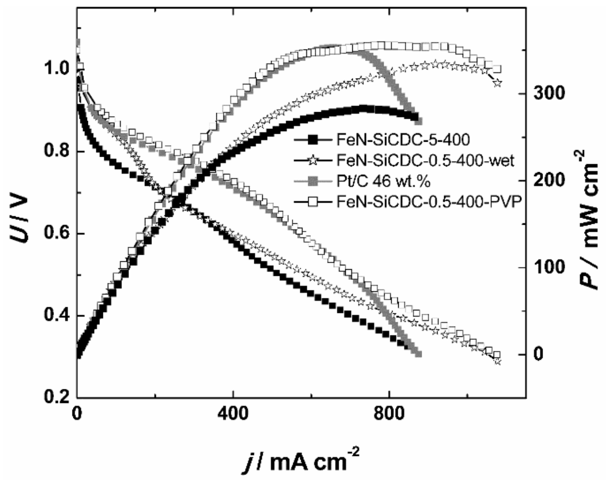

Figure 8. Single cell AEMFC polarization curves using FeN-SiCDC or a commercial Pt/C cathode catalyst (0.4 mg$_{Pt}$ cm^{-2}). The anode was a commercial PtRu/C catalyst with 0.8 mg$_{PtRu}$ cm^{-2} loading. T = 60 °C, cathode RH = 100%, anode RH = 82%, backpressure = 200 kPa.

Table 4. Kinetic current densities at 0.9 V vs RHE in the RDE setup and current densities at 0.9 V in AEMFC using the FeN-SiCDC catalysts.

Catalyst	$j_{k, 0.9 V, RDE}$ (mA cm^{-2})	$j_{0.9 V, MEA}$ (mA cm^{-2})
FeN-SiCDC-5-100	0.7	-
FeN-SiCDC-wet	2.2	-
FeN-SiCDC-5-400	2.9	10.3
FeN-SiCDC-5-800	0.6	-
FeN-SiCDC-0.5-400	1.2	-
FeN-SiCDC-0.5-400-wet	2.8	36.2
FeN-SiCDC-0.5-400-wet-PVP	3.8	52.0
Pt/C 46 wt.%	2.3	36.5

4. Conclusions

The effect of the conditions used during the ball-milling of the catalyst precursor, comprising silicon carbide-derived carbon, Phen and iron(II) acetate, on the electrocatalytic properties of the ORR catalysts was studied. Using a ZrO_2 ball size of 5 mm, the CDC particle size decreased as a result of the milling, but at high rotation rates, the negative effects induced by the milling overshadowed the positive ones. An optimal ball-milling rotation rate of 400 rpm was established. Decreasing the ball size to 0.5 mm ZrO_2 and wet ball-milling in the presence of PVP, the particle size was uniformly reduced to ca. 200 nm, without negatively impacting the microporous and BET areas. An increased surface nitrogen content and good dispersion of the Fe-based active sites (92% as Fe-N_x) were identified as reasons for increased activity in RDE mode. Due to the decreased particle size with no negative effects from the milling, the best catalyst achieved a current density of 52 mA cm^{-2} at 0.9 V and a maximum power density of 356 mW cm^{-2} in AEMFC, surpassing a commercial Pt/C cathode catalyst tested in the same conditions. This study presents, for the first time, a ball-milling method for reducing the particle size of Fe-N-CDC catalysts down to <1 μm while increasing their activity.

Declaration of interest

The authors declare that they have no known competing financial interests.

Acknowledgments

This work was supported by the Estonian Research Council [grants PRG723 and PRG4] and by institutional research funding [IUT34-14] of the Estonian Ministry of Education and Research. This research was also supported by the EU through the European Regional Development Fund [TK141, “Advanced materials and high-technology devices for energy recuperation systems”]. The French-Estonian PARROT program financed by the Estonian Research Council and Campus France is gratefully acknowledged.

References

[1] F.T. Wagner, B. Lakshmanan, M.F. Mathias, Electrochemistry and the future of the automobile, J. Phys. Chem. Lett. 1 (2010) 2204–2219. https://doi.org/10.1021/jz100553m.

[2] P.C.K. Vesborg, T.F. Jaramillo, Addressing the terawatt challenge: scalability in the supply of chemical elements for renewable energy, RSC Adv. 2 (2012) 7933. https://doi.org/10.1039/c2ra20839c.

[3] H.A. Gasteiger, N.M. Markovic, Just a dream or future reality?, Science 324 (2009) 48–49. https://doi.org/10.1126/science.1172083.

[4] M. Shao, Q. Chang, J.-P. Dodelet, R. Chenitz, Recent Advances in Electrocatalysts for Oxygen Reduction Reaction, Chem. Rev. 116 (2016) 3594–3657. https://doi.org/10.1021/acs.chemrev.5b00462.

[5] W.E. Mustain, Understanding how high-performance anion exchange membrane fuel cells were achieved: Component, interfacial, and cell-level factors, Curr. Opin. Electrochem. 12 (2018) 233–239. https://doi.org/10.1016/J.COELEC.2018.11.010.

[6] X. Peng, T.J. Omasta, E. Magliocca, L. Wang, J.R. Varcoe, W.E. Mustain, Nitrogen-doped Carbon-CoO_x Nanohybrids: A Precious Metal Free Cathode that Exceeds 1.0 W cm^{-2} Peak Power and 100 h Life in Anion-Exchange Membrane Fuel Cells, Angew. Chemie Int. Ed. 58 (2019) 1046–1051. https://doi.org/10.1002/anie.201811099.

[7] X. Peng, V. Kashyap, B. Ng, S. Kurungot, L. Wang, J. Varcoe, W. Mustain, High-Performing PGM-Free AEMFC Cathodes from Carbon-Supported Cobalt Ferrite Nanoparticles, Catalysts 9 (2019) 264. https://doi.org/10.3390/catal9030264.

[8] Y. Wang, Y. Yang, S. Jia, X. Wang, K. Lyu, Y. Peng, H. Zheng, X. Wei, H. Ren, L. Xiao, J. Wang, D.A. Muller, H.D. Abruña, B.J. Hwang, J. Lu, L. Zhuang, Synergistic Mn-Co catalyst outperforms Pt on high-rate oxygen reduction for alkaline polymer electrolyte fuel cells, Nat. Commun. 10 (2019) 1506. https://doi.org/10.1038/s41467-019-09503-4.

[9] S. Gottesfeld, D.R. Dekel, M. Page, C. Bae, Y. Yan, P. Zelenay, Y.S. Kim, Anion exchange membrane fuel cells: Current status and remaining challenges, J. Power Sources 375 (2018) 170–184. https://doi.org/10.1016/j.jpowsour.2017.08.010.

[10] H.A. Firouzjaie, W.E. Mustain, Catalytic Advantages, Challenges, and Priorities in Alkaline Membrane Fuel Cells, ACS Catal. 10 (2020) 225–234. https://doi.org/10.1021/acscatal.9b03892.

[11] N. Ramaswamy, S. Mukerjee, Fundamental mechanistic understanding of electrocatalysis of oxygen reduction on Pt and non-Pt surfaces: Acid versus alkaline media, Adv. Phys. Chem. 2012 (2012) 1–17. https://doi.org/10.1155/2012/491604.

[12] A. Sarapuu, E. Kibena-Põldsepp, M. Borghei, K. Tammeveski, Electrocatalysis of oxygen reduction on heteroatom-doped nanocarbons and transition metal-nitrogen-carbon catalysts for alkaline membrane fuel cells, J. Mater. Chem. A 6 (2018) 776–804.

https://doi.org/10.1039/C7TA08690C.

[13] Z. Chen, D. Higgins, A. Yu, L. Zhang, J. Zhang, A review on non-precious metal electrocatalysts for PEM fuel cells, Energy Environ. Sci. 4 (2011) 3167. https://doi.org/10.1039/c0ee00558d.

[14] T. Asefa, Metal-Free and Noble Metal-Free Heteroatom-Doped Nanostructured Carbons as Prospective Sustainable Electrocatalysts, Acc. Chem. Res. 49 (2016) 1873–1883. https://doi.org/10.1021/acs.accounts.6b00317.

[15] J. Liu, E. Li, M. Ruan, P. Song, W. Xu, Recent Progress on Fe/N/C Electrocatalysts for the Oxygen Reduction Reaction in Fuel Cells, Catalysts 5 (2015) 1167–1192. https://doi.org/10.3390/catal5031167.

[16] X. Wang, Z. Li, Y. Qu, T. Yuan, W. Wang, Y. Wu, Y. Li, Review of Metal Catalysts for Oxygen Reduction Reaction: From Nanoscale Engineering to Atomic Design, Chem 5 (2019) 1486–1511. https://doi.org/10.1016/J.CHEMPR.2019.03.002.

[17] A.A. Gewirth, J.A. Varnell, A.M. DiAscro, Nonprecious Metal Catalysts for Oxygen Reduction in Heterogeneous Aqueous Systems, Chem. Rev. 118 (2018) 2313–2339. https://doi.org/10.1021/acs.chemrev.7b00335.

[18] A. Zitolo, V. Goellner, V. Armel, M.T. Sougrati, T. Mineva, L. Stievano, E. Fonda, F. Jaouen, Identification of catalytic sites for oxygen reduction in iron- and nitrogen-doped graphene materials, Nat. Mater. 14 (2015) 937–942. https://doi.org/10.1038/nmat4367.

[19] Q. Jia, N. Ramaswamy, U. Tylus, K. Strickland, J. Li, A. Serov, K. Artyushkova, P. Atanassov, J. Anibal, C. Gumeci, S.C. Barton, M.T. Sougrati, F. Jaouen, B. Halevi, S. Mukerjee, Spectroscopic insights into the nature of active sites in iron–nitrogen–carbon electrocatalysts for oxygen reduction in acid, Nano Energy 29 (2016) 65–82. https://doi.org/10.1016/j.nanoen.2016.03.025.

[20] K. Artyushkova, A. Serov, S. Rojas-Carbonell, P. Atanassov, Chemistry of Multitudinous Active Sites for Oxygen Reduction Reaction in Transition Metal-Nitrogen-Carbon Electrocatalysts, J. Phys. Chem. C 119 (2015) 25917–25928. https://doi.org/10.1021/acs.jpcc.5b07653.

[21] U.I. Kramm, J. Herranz, N. Larouche, T.M. Arruda, M. Lefèvre, F. Jaouen, P. Bogdanoff, S. Fiechter, I. Abs-Wurmbach, S. Mukerjee, J.-P. Dodelet, Structure of the catalytic sites in Fe/N/C-catalysts for O2-reduction in PEM fuel cells, Phys. Chem. Chem. Phys. 14 (2012) 11673. https://doi.org/10.1039/c2cp41957b.

[22] H.T. Chung, D.A. Cullen, D. Higgins, B.T. Sneed, E.F. Holby, K.L. More, P. Zelenay, Direct atomic-level insight into the active sites of a high-performance PGM-free ORR catalyst., Science. 357 (2017) 479–484. https://doi.org/10.1126/science.aan2255.

[23] K. Strickland, E. Miner, Q. Jia, U. Tylus, N. Ramaswamy, W. Liang, M.T. Sougrati, F. Jaouen, S. Mukerjee, Highly active oxygen reduction non-platinum group metal electrocatalyst without direct metal-nitrogen coordination, Nat. Commun. 6 (2015) 7343. https://doi.org/10.1038/ncomms8343.

[24] M. Reda, H.A. Hansen, T. Vegge, DFT Study of the Oxygen Reduction Reaction on Carbon-Coated Iron and Iron Carbide, ACS Catal. 8 (2018) 10521–10529. https://doi.org/10.1021/acscatal.8b02167.

[25] S. Ratso, I. Kruusenberg, A. Sarapuu, M. Kook, P. Rauwel, R. Saar, J. Aruväli, K. Tammeveski, Electrocatalysis of oxygen reduction on iron- and cobalt-containing nitrogen-doped carbon nanotubes in acid media, Electrochim. Acta 218 (2016) 303–310.

https://doi.org/10.1016/j.electacta.2016.09.119.

[26] S. Ratso, M. Käärik, M. Kook, P. Paiste, V. Kisand, S. Vlassov, J. Leis, K. Tammeveski, Iron and Nitrogen Co-doped Carbide-Derived Carbon and Carbon Nanotube Composite Catalysts for Oxygen Reduction Reaction, ChemElectroChem 5 (2018) 1827–1836. https://doi.org/10.1002/celc.201800132.

[27] R. Sibul, E. Kibena-Põldsepp, S. Ratso, M. Kook, M. Käärik, M. Merisalu, P. Paiste, J. Leis, V. Sammelselg, K. Tammeveski, Nitrogen-doped carbon-based electrocatalysts synthesised by ball-milling, Electrochem. Commun. 93 (2018) 39–43. https://doi.org/10.1016/j.elecom.2018.05.027.

[28] K. Ping, A. Braschinsky, M. Alam, R. Bhadoria, V. Mikli, A. Mere, J. Aruväli, P. Paiste, S. Vlassov, M. Kook, M. Rähn, V. Sammelselg, K. Tammeveski, N. Kongi, P. Starkov, Fused Hybrid Linkers for Metal–Organic Framework-Derived Bifunctional Oxygen Electrocatalysts, ACS Appl. Energy Mater. 3 (2020) 152–157. https://doi.org/10.1021/acsaem.9b02039.

[29] W. Wang, Q. Jia, S. Mukerjee, S. Chen, Recent Insights into the Oxygen-Reduction Electrocatalysis of Fe/N/C Materials, ACS Catal. 9 (2019) 10126–10141. https://doi.org/10.1021/acscatal.9b02583.

[30] Y. Hu, J.O. Jensen, W. Zhang, L.N. Cleemann, W. Xing, N.J. Bjerrum, Q. Li, Hollow spheres of iron carbide nanoparticles encased in graphitic layers as oxygen reduction catalysts, Angew. Chem. Int. Ed. 53 (2014) 3675–3679. https://doi.org/10.1002/anie.201400358.

[31] H. Xu, D. Cheng, D. Cao, X.C. Zeng, A universal principle for a rational design of single-atom electrocatalysts, Nat. Catal. 1 (2018) 339–348. https://doi.org/10.1038/s41929-018-0063-z.

[32] U. Tylus, Q. Jia, K. Strickland, N. Ramaswamy, A. Serov, P. Atanassov, S. Mukerjee, Elucidating oxygen reduction active sites in pyrolyzed metal-nitrogen coordinated non-precious-metal electrocatalyst systems, J. Phys. Chem. C 118 (2014) 8999–9008. https://doi.org/10.1021/jp500781v.

[33] I. Matanovic, K. Artyushkova, P. Atanassov, Understanding PGM-free catalysts by linking density functional theory calculations and structural analysis: Perspectives and challenges, Curr. Opin. Electrochem. 9 (2018) 137-144. https://doi.org/10.1016/j.coelec.2018.03.009.

[34] A. Ferre-Vilaplana, E. Herrero, Understanding the chemisorption-based activation mechanism of the oxygen reduction reaction on nitrogen-doped graphitic materials, Electrochim. Acta 204 (2016) 245–254. https://doi.org/10.1016/J.ELECTACTA.2016.04.039.

[35] N. Ramaswamy, U. Tylus, Q. Jia, S. Mukerjee, Activity descriptor identification for oxygen reduction on nonprecious electrocatalysts: Linking surface science to coordination chemistry, J. Am. Chem. Soc. 135 (2013) 15443–15449. https://doi.org/10.1021/ja405149m.

[36] J. Li, Q. Jia, S. Mukerjee, M.-T. Sougrati, G. Drazic, A. Zitolo, F. Jaouen, J. Li, Q. Jia, S. Mukerjee, M.-T. Sougrati, G. Drazic, A. Zitolo, F. Jaouen, The Challenge of Achieving a High Density of Fe-Based Active Sites in a Highly Graphitic Carbon Matrix, Catalysts 9 (2019) 144. https://doi.org/10.3390/catal9020144.

[37] J. Li, F. Jaouen, Structure and activity of metal-centered coordination sites in pyrolyzed metal–nitrogen–carbon catalysts for the electrochemical reduction of O2, Curr. Opin. Electrochem. 9 (2018) 198–206. https://doi.org/10.1016/J.COELEC.2018.03.039.

[38] F. Jaouen, M. Lefèvre, J.P. Dodelet, M. Cai, Heat-treated Fe/N/C catalysts for O2 electroreduction: Are active sites hosted in micropores?, J. Phys. Chem. B 110 (2006) 5553–

5558. https://doi.org/10.1021/jp057135h.

[39] T. Soboleva, X. Zhao, K. Malek, Z. Xie, T. Navessin, S. Holdcroft, On the micro-, meso-, and macroporous structures of polymer electrolyte membrane fuel cell catalyst layers, ACS Appl. Mater. Interfaces 2 (2010) 375–384. https://doi.org/10.1021/am900600y.

[40] B. Britton, S. Holdcroft, The Control and Effect of Pore Size Distribution in AEMFC Catalyst Layers, J. Electrochem. Soc. 163 (2016) F353–F358. https://doi.org/10.1149/2.0421605jes.

[41] J. Shui, C. Chen, L. Grabstanowicz, D. Zhao, D.-J. Liu, Highly efficient nonprecious metal catalyst prepared with metal–organic framework in a continuous carbon nanofibrous network, Proc. Natl. Acad. Sci. U.S.A. 112 (2015) 10629–10634. https://doi.org/10.1073/pnas.1507159112.

[42] Y. Gogotsi, A. Nikitin, H. Ye, W. Zhou, J.E. Fischer, B. Yi, H.C. Foley, M.W. Barsoum, Nanoporous carbide-derived carbon with tunable pore size, Nat. Mater. 2 (2003) 591–594. https://doi.org/10.1038/nmat957.

[43] M. Käärik, U. Maran, M. Arulepp, A. Perkson, J. Leis, Quantitative Nano-Structure–Property Relationships for the Nanoporous Carbon: Predicting the Performance of Energy Storage Materials, ACS Appl. Energy Mater. 1 (2018) 4016–4024. https://doi.org/10.1021/acsaem.8b00708.

[44] S. Ratso, N. Ranjbar Sahraie, M.T. Sougrati, M. Käärik, M. Kook, R. Saar, P. Paiste, Q. Jia, J. Leis, S. Mukerjee, F. Jaouen, K. Tammeveski, Synthesis of highly-active Fe-N-C catalysts for PEMFC with carbide-derived carbons, J. Mater. Chem. A 6 (2018) 14663–14674. https://doi.org/10.1039/c8ta02325e.

[45] P. Teppor, R. Jäger, E. Härk, U. Joost, I. Tallo, P. Paiste, K. Kirsimäe, E. Lust, Oxygen Reduction Reaction on Nitrogen and Cobalt Modified Silicon Carbide Derived Carbon in Acidic Media, ECS Trans. 85 (2018) 855–863. https://doi.org/10.1149/08513.0855ecst.

[46] S. Ratso, M. Käärik, M. Kook, P. Paiste, J. Aruväli, S. Vlassov, V. Kisand, J. Leis, A.M. Kannan, K. Tammeveski, High performance catalysts based on Fe/N co-doped carbide-derived carbon and carbon nanotube composites for oxygen reduction reaction in acid media, Int. J. Hydrogen Energy 44 (2019) 12636–12648. https://doi.org/10.1016/j.ijhydene.2018.11.080.

[47] R. Jäger, P.E. Kasatkin, E. Härk, P. Teppor, T. Romann, R. Härmas, I. Tallo, U. Mäeorg, U. Joost, P. Paiste, K. Kirsimäe, E. Lust, The effect of N precursors in Fe-N/C type catalysts based on activated silicon carbide derived carbon for oxygen reduction activity at various pH values, J. Electroanal. Chem. 823 (2018) 593–600. https://doi.org/10.1016/j.jelechem.2018.06.040.

[48] S. Ratso, I. Kruusenberg, M. Käärik, M. Kook, L. Puust, R. Saar, J. Leis, K. Tammeveski, Highly efficient transition metal and nitrogen co-doped carbide-derived carbon electrocatalysts for anion exchange membrane fuel cells, J. Power Sources 375 (2018) 233–243. https://doi.org/10.1016/j.jpowsour.2017.08.046.

[49] S. Ratso, M.T. Sougrati, M. Käärik, M. Merisalu, M. Rähn, V. Kisand, A. Kikas, P. Paiste, J. Leis, V. Sammelselg, F. Jaouen, K. Tammeveski, Effect of Ball-Milling on the Oxygen Reduction Reaction Activity of Iron and Nitrogen Co-doped Carbide-Derived Carbon Catalysts in Acid Media, ACS Appl. Energy Mater. 2 (2019) 7952–7962. https://doi.org/10.1021/acsaem.9b01430.

[50] S. Brunauer, P.H. Emmett, E. Teller, Adsorption of Gases in Multimolecular Layers, J. Am. Chem. Soc. 60 (1938) 309–319. https://doi.org/10.1021/ja01269a023.

[51] B. Ravel, M. Newville, ATHENA, ARTEMIS, HEPHAESTUS: data analysis for X-ray absorption

spectroscopy using IFEFFIT, J. Synchrotron Radiat. 12 (2005) 537–541. https://doi.org/10.1107/S0909049505012719.

[52] A.G. Wright, J. Fan, B. Britton, T. Weissbach, H.-F. Lee, E.A. Kitching, T.J. Peckham, S. Holdcroft, Hexamethyl-p-terphenyl poly(benzimidazolium): a universal hydroxide-conducting polymer for energy conversion devices, Energy Environ. Sci. 9 (2016) 2130–2142. https://doi.org/10.1039/C6EE00656F.

[53] S. Ratso, I. Kruusenberg, M. Käärik, M. Kook, R. Saar, P. Kanninen, T. Kallio, J. Leis, K. Tammeveski, Transition metal-nitrogen co-doped carbide-derived carbon catalysts for oxygen reduction reaction in alkaline direct methanol fuel cell, Appl. Catal. B Environ. 219 (2017) 276–286. https://doi.org/10.1016/j.apcatb.2017.07.036.

[54] A. Nouri, C. Wen, Surfactants in Mechanical Alloying/Milling: A Catch-22 Situation, Crit. Rev. Solid State Mater. Sci. 39 (2014) 81–108. https://doi.org/10.1080/10408436.2013.808985.

[55] M. Lefèvre, E. Proietti, F. Jaouen, J.P. Dodelet, Iron-Based catalysts with improved oxygen reduction activity in polymer electrolyte fuel cells, Science 324 (2009) 71–74. https://doi.org/10.1126/science.1170051.

[56] J. Li, S. Ghoshal, W. Liang, M.-T. Sougrati, F. Jaouen, B. Halevi, S. McKinney, G. McCool, C. Ma, X. Yuan, Z.-F. Ma, S. Mukerjee, Q. Jia, Structural and mechanistic basis for the high activity of Fe–N–C catalysts toward oxygen reduction, Energy Environ. Sci. 9 (2016) 2418–2432. https://doi.org/10.1039/C6EE01160H.

[57] J. Tian, A. Morozan, M.T. Sougrati, M. Lefèvre, R. Chenitz, J.-P. Dodelet, D. Jones, F. Jaouen, Optimized Synthesis of Fe/N/C Cathode Catalysts for PEM Fuel Cells: A Matter of Iron-Ligand Coordination Strength, Angew. Chem. Int. Ed. 52 (2013) 6867–6870. https://doi.org/10.1002/anie.201303025.

[58] J. Sanetuntikul, S. Shanmugam, High pressure pyrolyzed non-precious metal oxygen reduction catalysts for alkaline polymer electrolyte membrane fuel cells, Nanoscale 7 (2015) 7644–7650. https://doi.org/10.1039/C5NR00311C.

[59] J. Guo, H. He, D. Chu, R. Chen, OH--Binding Effects on Metallophthalocyanine Catalysts for O2 Reduction Reaction in Anion Exchange Membrane Fuel Cells, Electrocatalysis 3 (2012) 252–264. https://doi.org/10.1007/s12678-012-0106-1.

[60] H.A. Miller, M. Bellini, W. Oberhauser, X. Deng, H. Chen, Q. He, M. Passaponti, M. Innocenti, R. Yang, F. Sun, Z. Jiang, F. Vizza, Heat treated carbon supported iron(ii)phthalocyanine oxygen reduction catalysts: elucidation of the structure–activity relationship using X-ray absorption spectroscopy, Phys. Chem. Chem. Phys. 18 (2016) 33142–33151. https://doi.org/10.1039/C6CP06798K.

[61] P. Song, Y. Zhang, J. Pan, L. Zhuang, W. Xu, Cheap carbon black-based high-performance electrocatalysts for oxygen reduction reaction, Chem. Commun. 51 (2015) 1972–1975. https://doi.org/10.1039/c4cc07677j.

[62] H. Lee, M.J. Kim, T. Lim, Y.E. Sung, H.J. Kim, H.N. Lee, O.J. Kwon, Y.H. Cho, A facile synthetic strategy for iron, aniline-based non-precious metal catalysts for polymer electrolyte membrane fuel cells, Sci. Rep. 7 (2017) 5396. https://doi.org/10.1038/s41598-017-05830-y.

[63] H.C. Huang, Y.C. Lin, S.T. Chang, C.C. Liu, K.C. Wang, H.P. Jhong, J.F. Lee, C.H. Wang, Effect of a sulfur and nitrogen dual-doped Fe-N-S electrocatalyst for the oxygen reduction reaction, J. Mater. Chem. A 5 (2017) 19790–19799. https://doi.org/10.1039/c7ta05030e.

[64] V.M. Dhavale, S.K. Singh, A. Nadeema, S.S. Gaikwad, S. Kurungot, Nanocrystalline Fe-Fe2O3 particle-deposited N-doped graphene as an activity-modulated Pt-free electrocatalyst for oxygen reduction reaction, Nanoscale 7 (2015) 20117–20125. https://doi.org/10.1039/c5nr04929f.

[65] C. Chen, X.-D. Yang, Z.-Y. Zhou, Y.-J. Lai, M. Rauf, Y. Wang, J. Pan, L. Zhuang, Q. Wang, Y.-C. Wang, N. Tian, X.-S. Zhang, S.-G. Sun, Aminothiazole-derived N,S,Fe-doped graphene nanosheets as high performance electrocatalysts for oxygen reduction, Chem. Commun. 51 (2015) 17092–17095. https://doi.org/10.1039/C5CC06562C.

[66] I. Kruusenberg, L. Matisen, Q. Shah, A.M. Kannan, K. Tammeveski, Non-platinum cathode catalysts for alkaline membrane fuel cells, Int. J. Hydrogen Energy 37 (2012) 4406–4412. https://doi.org/10.1016/j.ijhydene.2011.11.143.

[67] S.M. Unni, S. Ramadas, R. Illathvalappil, S.N. Bhange, S. Kurungot, Surface-modified single wall carbon nanohorn as an effective electrocatalyst for platinum-free fuel cell cathodes, J. Mater. Chem. A 3 (2015) 4361–4367. https://doi.org/10.1039/c4ta05092d.

[68] J. Sanetuntikul, C. Chuaicham, Y.-W. Choi, S. Shanmugam, Investigation of hollow nitrogen-doped carbon spheres as non-precious Fe–N_4 based oxygen reduction catalysts, J. Mater. Chem. A 3 (2015) 15473–15481. https://doi.org/10.1039/C5TA02677F.

[69] G.A. Ferrero, K. Preuss, A. Marinovic, A.B. Jorge, N. Mansor, D.J.L. Brett, A.B. Fuertes, M. Sevilla, M.M. Titirici, Fe-N-Doped Carbon Capsules with Outstanding Electrochemical Performance and Stability for the Oxygen Reduction Reaction in Both Acid and Alkaline Conditions, ACS Nano 10 (2016) 5922–5932. https://doi.org/10.1021/acsnano.6b01247.

[70] D.Y. Chung, M.J. Kim, N. Kang, J.M. Yoo, H. Shin, O.H. Kim, Y.E. Sung, Low-Temperature and Gram-Scale Synthesis of Two-Dimensional Fe-N-C Carbon Sheets for Robust Electrochemical Oxygen Reduction Reaction, Chem. Mater. 29 (2017) 2890–2898. https://doi.org/10.1021/acs.chemmater.6b05113.

[71] R. Gokhale, Y. Chen, A. Serov, K. Artyushkova, P. Atanassov, Novel dual templating approach for preparation of highly active Fe-N-C electrocatalyst for oxygen reduction, Electrochim. Acta 224 (2017) 49–55. https://doi.org/10.1016/j.electacta.2016.12.052.

[72] Y. Mun, M.J. Kim, S.A. Park, E. Lee, Y. Ye, S. Lee, Y.T. Kim, S. Kim, O.H. Kim, Y.H. Cho, Y.E. Sung, J. Lee, Soft-template synthesis of mesoporous non-precious metal catalyst with Fe-Nx/C active sites for oxygen reduction reaction in fuel cells, Appl. Catal. B Environ. 222 (2018) 191–199. https://doi.org/10.1016/j.apcatb.2017.10.015.

[73] M.M. Hossen, K. Artyushkova, P. Atanassov, A. Serov, Synthesis and characterization of high performing Fe-N-C catalyst for oxygen reduction reaction (ORR) in Alkaline Exchange Membrane Fuel Cells, J. Power Sources 375 (2018) 214–221. https://doi.org/10.1016/j.jpowsour.2017.08.036.

[74] R. Praats, M. Käärik, A. Kikas, V. Kisand, J. Aruväli, P. Paiste, M. Merisalu, J. Leis, V. Sammelselg, J.H. Zagal, S. Holdcroft, N. Nakashima, K. Tammeveski, Electrocatalytic oxygen reduction reaction on iron phthalocyanine-modified carbide-derived carbon/carbon nanotube composite electrocatalysts, Electrochim. Acta 334 (2020) 135575. https://doi.org/10.1016/j.electacta.2019.135575.

[75] J. Yang, J. Tao, T. Isomura, H. Yanagi, I. Moriguchi, N. Nakashima, A comparative study of iron phthalocyanine electrocatalysts supported on different nanocarbons for oxygen reduction

reaction, Carbon 145 (2019) 565–571. https://doi.org/10.1016/j.carbon.2019.01.022.

[76] Y. Zhao, L. Liao, G. Yu, P. Wei, J. Liu, B-Doped Fe/N/C Porous Catalyst for High-Performance Oxygen Reduction in Anion-Exchange Membrane Fuel Cells, ChemElectroChem 6 (2019) 1754–1760. https://doi.org/10.1002/celc.201801688.

[77] S.H. Lee, J. Kim, D.Y. Chung, J.M. Yoo, H.S. Lee, M.J. Kim, B.S. Mun, S.G. Kwon, Y.-E. Sung, T. Hyeon, Design Principle of Fe–N–C Electrocatalysts: How to Optimize Multimodal Porous Structures?, J. Am. Chem. Soc. 141 (2019) 2035–2045. https://doi.org/10.1021/jacs.8b11129.

[78] J. Woo, S.Y. Yang, Y.J. Sa, W.Y. Choi, M.H. Lee, H.W. Lee, T.J. Shin, T.Y. Kim, S.H. Joo, Promoting Oxygen Reduction Reaction Activity of Fe-N/C Electrocatalysts by Silica-Coating-Mediated Synthesis for Anion-Exchange Membrane Fuel Cells, Chem. Mater. 30 (2018) 6684–6701. https://doi.org/10.1021/acs.chemmater.8b02117.

[79] H. Zhang, S. Zhang, Y. Wang, J. Si, Y. Chen, L. Zhuang, S. Chen, Boosting the Performance of Iron-Phthalocyanine as Cathode Electrocatalyst for Alkaline Polymer Fuel Cells Through Edge-Closed Conjugation, ACS Appl. Mater. Interfaces 10 (2018) 28664–28671. https://doi.org/10.1021/acsami.8b09074.

[80] R. Sibul, E. Kibena-Põldsepp, S. Ratso, M. Kook, M.T. Sougrati, M. Käärik, M. Merisalu, J. Aruväli, P. Paiste, A. Treshchalov, J. Leis, V. Kisand, V. Sammelselg, S. Holdcroft, F. Jaouen, K. Tammeveski, Iron- and Nitrogen-Doped Graphene-Based Catalysts for Fuel Cell Applications, ChemElectroChem 7 (2020) 1739–1747. https://doi.org/10.1002/celc.202000011.

[81] R. Soni, S.N. Bhange, S. Kurungot, A 3-D nanoribbon-like Pt-free oxygen reduction reaction electrocatalyst derived from waste leather for anion exchange membrane fuel cells and zinc-air batteries, Nanoscale 11 (2019) 7893–7902. https://doi.org/10.1039/C9NR00977A.

[82] Y.J. Sa, D.J. Seo, J. Woo, J.T. Lim, J.Y. Cheon, S.Y. Yang, J.M. Lee, D. Kang, T.J. Shin, H.S. Shin, H.Y. Jeong, C.S. Kim, M.G. Kim, T.Y. Kim, S.H. Joo, A General Approach to Preferential Formation of Active Fe-Nx Sites in Fe-N/C Electrocatalysts for Efficient Oxygen Reduction Reaction, J. Am. Chem. Soc. 138 (2016) 15046–15056. https://doi.org/10.1021/jacs.6b09470.

[83] M. Mooste, E. Kibena-Põldsepp, V. Vassiljeva, A. Kikas, M. Käärik, J. Kozlova, V. Kisand, M. Külaviir, S. Cavaliere, J. Leis, A. Krumme, V. Sammelselg, S. Holdcroft, K. Tammeveski, Electrospun Polyacrylonitrile-Derived Co or Fe Containing Nanofibre Catalysts for Oxygen Reduction Reaction at the Alkaline Membrane Fuel Cell Cathode, ChemCatChem. 12 (2020) 4568–4581. https://doi.org/10.1002/cctc.202000658.

[84] P.G. Santori, F.D. Speck, S. Cherevko, H.A. Firouzjaie, X. Peng, W.E. Mustain, F. Jaouen, High Performance FeNC and Mn-oxide/FeNC Layers for AEMFC Cathodes, J. Electrochem. Soc. 167 (2020) 134505. https://doi.org/10.1149/1945-7111/abb7e0.

[85] K. Kisand, A. Sarapuu, D. Danilian, A. Kikas, V. Kisand, M. Rähn, A. Treshchalov, M. Käärik, M. Merisalu, P. Paiste, J. Aruväli, J. Leis, V. Sammelselg, S. Holdcroft, K. Tammeveski, Transition metal-containing nitrogen-doped nanocarbon catalysts derived from 5-methylresorcinol for anion exchange membrane fuel cell application, J. Colloid Interface Sci. 584 (2021) 263–274. https://doi.org/10.1016/j.jcis.2020.09.114.

[86] S.T. Thompson, D. Peterson, D. Ho, D. Papageorgopoulos, Perspective—The Next Decade of AEMFCs: Near-Term Targets to Accelerate Applied R&D, J. Electrochem. Soc. 167 (2020) 084514. https://doi.org/10.1149/1945-7111/ab8c88.